Chiral Assemblies of Laser-Printed Micropillars Directed by Asymmetrical Capillary Force

Yanlei Hu,* Hongwei Yuan, Shunli Liu, Jincheng Ni, Zhaoxin Lao, Chen Xin, Deng Pan, Yiyuan Zhang, Wulin Zhu, Jiawen Li, Dong Wu,* and Jiaru Chu

Artificial microstructures composed of chiral building blocks are of great significance in the fields of optics and mechanics. Here, it is shown that highly ordered chiral structures can be spontaneously assembled by a meniscus-directed capillary force arising in an evaporating liquid. The chirality is facilitated by rationally breaking the intrinsic symmetry in the unit cells through cooperative control of the geometry and spatial topology of the micropillars. The interfacial dynamics of the assembly process are studied to show that the sequential self-organization of the micropillars is influenced by the geometries, stiffness, and spatial arrangements. A diversity of chiral assemblies with controlled handedness is yielded by varying the pillar number, height, cross-section, laser power, and spatial topology. Lastly, the differential reflectance of light carrying opposite orbital angular momentums on the assembled chiral architectures are investigated, showcasing their potential in the field of chiral photonics concerning enantioselective response and exceptional optical functions.

Chirality is a marvelous phenomenon of omnipresence spanning from natural world to scientific fields. Natural examples include giant spiral galaxies,[1] curled plant tendril[2] and helical polynucleotide[3] with various scales ranging from astronomical distance to molecular level. Rationally designed artificial chiral architectures have found broad research interest in both photonic[4] and mechanical[5] domains due to their nontrivial interaction with light and elastic waves, which unfolds significant possibilities of human-made chiral structures in novel devices and systems that are previously inaccessible with ordinary materials.

So far, the fabrication strategies for chiral microstructures can be cataloged into top-down and bottom-up approaches according to the opposing ways to treat the base materials. Top-down approaches such as lithography are developed as designer tools with the ability to prepare structures in a

controlled manner.[6] However, top-down techniques are not scalable and most of them suffer from time-consuming and labor-intensive procedures, thus hindering their potential applications. In particular, chiral microstructures can be rapidly fabricated via single exposure of modulated femtosecond laser focus.[7] The geometry is strictly determined by the achievable structured focus and the resulting surface quality is rather poor. In contrast, bottom-up approach offers a cost-efficient and scalable alternative for creating hierarchical nanostructures through sequential self-assembly of subunits made from disparate materials such as copolymers,[8] peptides,[9] nanoparticles[10] and DNA tetrahedral.[11] Unfortunately, exact control over the geometries, spatial arrangements, regularity and helicity is very difficult owing to the inherent feature of the spontaneous self-assembly process. Recent progress in hybrid fabrication integrating top-down and bottom-up approaches offers promise to overcome some of the aforementioned limitations.[12] Particularly, capillary force driven self-assembly by mediating the elastocapillary interaction has attracted considerable interests because it affords the distinctive advantages of simplicity and scalability,[13] and to a certain extent, has been employed in hybrid fabrication strategies. Lithography-based fabrication of mesoscale bristles has been realized and highly ordered helical clusters have been yielded by exploiting the elastocapillary coalescence.[14] However, the achieved chirality of an individual cluster is random due to the rotationally symmetric circular fibrils. Although the specific chiral rearrangement can be obtained by rendering rectangular in cross-section, the tunability of chirality is still limited. Nanopillars at the 10 nm scale are realized using electron-beam lithography and then driven to self-assembly by capillary force induced nanocohesion.[15] Large-area patterned micropillars are prepared and assembled using multibeam interference lithography combined with subsequent capillary force during solution evaporation.[16] Our previous work has revealed that capillary force can be explored to drive the straight pillars to generate hierarchical microstructures with high controllability.[17] Nevertheless, neither of them can realize controlled chiral structures due to the fact that capillary force is very difficult to harness at the microscale Therefore, development of a facile, controllable and efficient methodology for the preparation of functional chiral structures is highly desirable.

Prof. Y. Hu, H. Yuan, S. Liu, Dr. J. Ni, Dr. Z. Lao, C. Xin, D. Pan, Y. Zhang, W. Zhu, Prof. J. Li, Prof. D. Wu, Prof. J. Chu
Hefei National Laboratory for Physical Sciences at the Microscale
CAS Key Laboratory of Mechanical Behavior and Design of Materials
Department of Precision Machinery and Precision Instrumentation
University of Science and Technology of China
Hefei, Anhui 230027, China
E-mail: huyl@ustc.edu.cn; dongwu@ustc.edu.cn

The ORCID identification number(s) for the author(s) of this article can be found under https://doi.org/10.1002/adma.202002356.

Herein, femtosecond laser printing is combined with capillarity-induced self-assembly to yield mesoscale chiral architectures with fine designability and tailorability. The controlled chirality is enabled by intentionally breaking the geometric symmetry of the laser-printed subunits through cooperative control over the micropillar geometry and spatial arrangements. The dynamics of the chiral assembly formation is investigated and different assembling modes are experimentally observed. Diverse chiral assemblies are realized by taking advantage of the flexibility of top-down laser printing technique. Significant optical vortical differential reflectance is observed arising from the strong coupling between assembled chiral enantiomers and optical helical wave front, opening up the potential applications for the chiroptical spectroscopy in material science and biology.

As illustrated in **Figure 1**a, micropillars are handily fabricated by focusing a femtosecond laser beam into a photoresist using an objective lens. The sample is anchored on a 3D nanotranslation stage to precisely control the geometries and spatial locations of the micropillars. The detailed experimental process is described in the Experimental Section. Compared with other lithography methods, the laser printing strategy possesses the advantage of simplicity and 3D flexibility. Batch creation of microstructures with great geometric diversity can be realized in a straightforward fashion.

After photopolymerization, the processed sample is developed in 1-propanol to dissolve unreacted and less-polymerized monomers or oligomers. Eventually, the solidified micropillar arrays are left on the substrate. In the later stage of the developing process, a meniscus is formed which is determined by the three-phase contact line when the liquid evaporates and reaches the top of the micropillars (Figure 1b). Capillary force directed by the meniscus can drag the micropillar to bend. As previously reported,[17] micropillars with round cross-section in a square array can bend to the center and assembles into a symmetric achiral unit cell by laser printing capillary-assisted self-assembly (LPCS) approach, as shown in Figure 1c. However, it is quite challenging to realize chiral microstructures in a controllable manner because of the symmetrical capillary
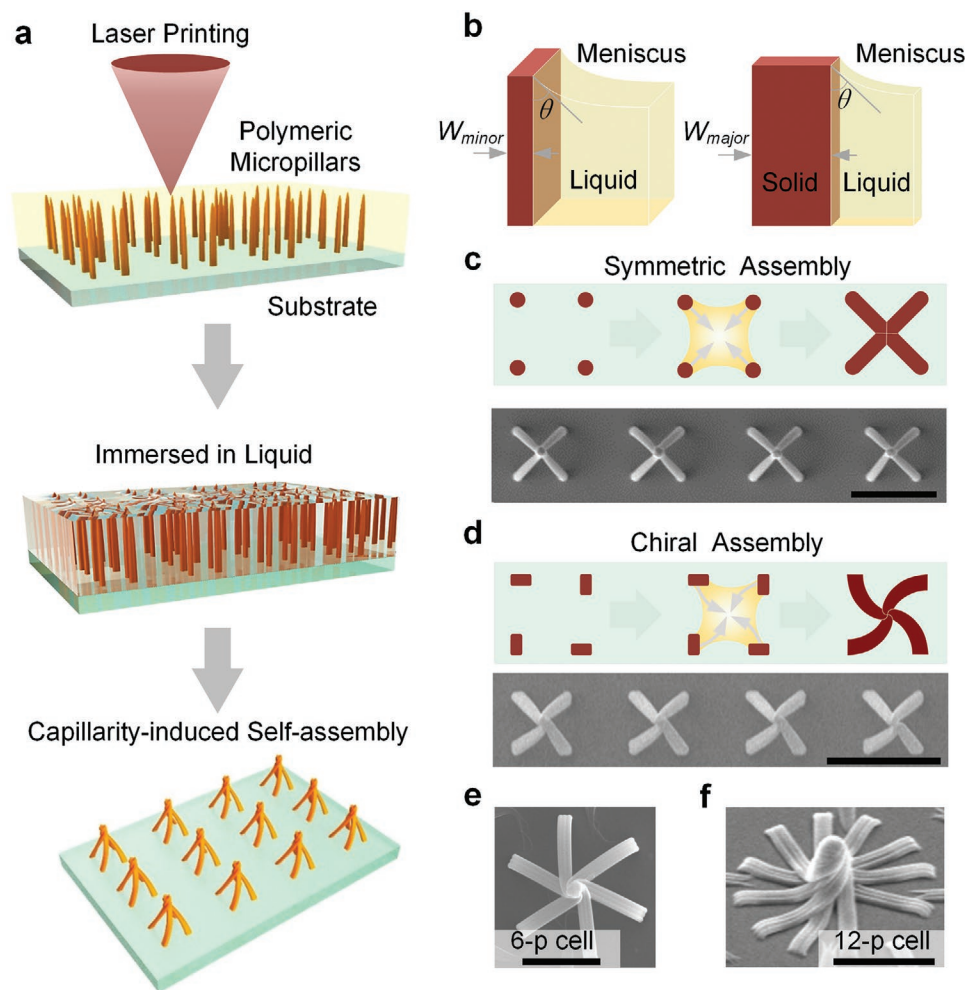
Figure 1. Preparation of deterministic chiral structures by combining laser printing and capillarity-induced self-assembly. a) Laser printing of micropillars and the subsequent self-assembly. b) Anisotropic capillary forces induced by the meniscus on the rectangular micropillars. The asymmetric capillary force leads to the creation of chiral assemblies. c) Schematic of the formation of symmetric assembly with square unit cells of round micropillars, and corresponding experimental result. d) Schematic of the formation of chiral assembly with unit cells of anisotropic micropillars with predesigned spatial arrangement, and corresponding experimental result. e,f) Typical chiral assemblies with 6 (e) and 12 (f) micropillars. Scale bars: 10 µm.

force exerted on the micropillars. For this purpose, it is desired to control capillary force at the microscale through inventive design of building units.

In order to generate the asymmetric assemblies with controllable chirality, the spatial arrangement of the rectangular micropillars inside a cell is designed to have an intrinsic helicity (Figure 1d). The micropillar of rectangular cross-section holds anisotropic elastic standing forces along the major axis and the minor axis. Meanwhile, the capillary forces exerted on the micropillar are mediated with different magnitudes and directions, which eventually leads to the creation of spiral assemblies.

The self-assembled microstructures are a result of competition between capillary force (F_C) and standing force (F_S). The capillary force directed by the meniscus along the direction of the minor axis and the major axis are given by

$$F_{C(minor,major)} \approx \frac{\gamma h w_{(major,minor)} \cos\theta}{d} \tag{1}$$

where h, w_{major}, and w_{minor} are the height, width of major and minor axes of the micropillar, respectively, γ is the liquid–solid interfacial tension, θ is the contact angle between liquid and the micropillars, and d is the distance between adjacent micropillars. Obviously, the capillary forces exerted on the anisotropic micropillar are different in the two orthogonal directions: $F_{C(minor)} > F_{C(major)}$. The critical standing force, derived from the instinctive elastic restoring force of micropillars while bending, occurs when two adjacent micropillars contact at their tips. Similarly, the critical standing force along the direction of the minor axis and the major axis can be respectively described by

$$F_{S(minor)} \approx \frac{E w_{minor}^3 w_{major} d}{h^3} \tag{2}$$

$$F_{S(major)} \approx \frac{E w_{major}^3 w_{minor} d}{h^3} \tag{3}$$

where E is Young's modulus of the micropillar. For a micropillar with an anisotropic rectangular cross-section, it is evident that the critical standing forces along the direction of the minor axis is much smaller than that along the major axis: $F_{S(minor)} < F_{S(major)}$. During the liquid evaporation process, the micropillars can bend along a specific direction when the capillary force is larger than the critical standing force. According to the discussion above, the micropillar bends along the minor axis more easily due to the larger capillary driving force and the smaller critical standing force. More importantly, as a result of the net capillary force between multiple micropillars inside a unit cell, the micropillar bends toward the center of the cell, as illustrated in Figure 1d.

During the anisotropic micropillar bends toward the cell center, a spontaneous curling occurred because the base is fixed onto the substrate. The tendency makes the micropillars wound around each other into a helix. From the minimal energy model's point of view, the total energy of the micropillars comprises the elastic energy caused by bending and the adhesive energy caused by twining contact. The elastic energy is a positive value proportional to the bending stiffness (Er^4), pillar height and inversely proportional to the helix radius. Meanwhile, the

adhesive energy is a negative value whose magnitude is proportional to the adhesive energy per unit area, contact width, the pillar height, and a root function of the helix pitch and radius.[14] Therefore, for soft micropillars, minimizing the total energy leads to a definite set of helix parameters (pitch and radius).

In this experiment, the parameters γ, r, and θ are fixed, h, d, w, and E can be properly adjusted according to the design to explore the formation of microstructures under different parameters. The additional distance (Δd) between two adjacent cells is selected large enough in order to ignore the influence between each other. It can be predicted that diverse spiral-controllable microstructure array can be formed when the cross-section and 2D spatial distribution of micropillars are cooperative controlled as scheme shown in the Figure 1d. Typical examples of 6-pillar and 12-pillar chiral assemblies are shown in Figure 1e,f.

According to the experimental observation, there are three kinds of results (upstanding, collapsed, or self-assembled) of micropillars in a square cell under the capillary force. For the symmetric micropillars of round cross-section, there is only one common form of the self-assembled four-pillar microstructures, in which the tips of the micropillars are in contact with each other, as shown in the scanning electron microscopy (SEM) image of the first row in the Figure 1c. In contrast, nontrivial assembly modes can be created by the micropillars of anisotropic cross-section and chiral spatial arrangement in a four-pillar cell under the induction of meniscus-directed capillary force. As shown in **Figure 2**a,b and Figures S1 and S2 (Supporting Information), highly ordered chiral assemblies with different morphologies, including helical folding buckles (Type IV) and pinwheel-like spiral assemblies (Type III) can be formed with controlled handedness. Definitely, as the same as the symmetric round micropillars, other types including upright pillars (Type I), and two-pillar assembly (Type II) can be generated when the micropillars are too low or too stiff. The morphologies of these four modes are summarized in Figure 2c. Moreover, collapsed messy state (Type V) can be found when the pillar is too high or too soft (Figures S1 and S3, Supporting Information). The height of the micropillars is readily controlled by the laser printing process, and the stiffness of the micropillars is controlled by tuning the laser power. The higher laser power gives rise to the higher stiffness.

The dependence of assembly modes on the two significant parameters, the height h and the laser processing power (P), is studied. Figure 2d shows the phase diagram for the assembling modes with varying pillar height and laser power. The corresponding typical optical images are shown in Figure S3 (Supporting Information). As expected, when the laser processing power is high along with small height of micropillars, the stiffness of the micropillar is so high that the capillary force is insufficient to compete with the standing force, causing the micropillars to maintain the upright state. In contrast, when the laser power is low along with high height of micropillars, the micropillars are easily disturbed and collapsed, eventually exhibiting a messy state. Only in the regime with appropriate parameter sets, the desired chiral assemblies (Type II, Type III, and Type IV) can be generated with controlled handedness. It should be noted that the phase diagram for the assembly modes is drawn based on the majority of the architecture forms. There

**ADVANCED
SCIENCE NEWS**

www.advancedsciencenews.com

**ADVANCED
MATERIALS**

www.advmat.de
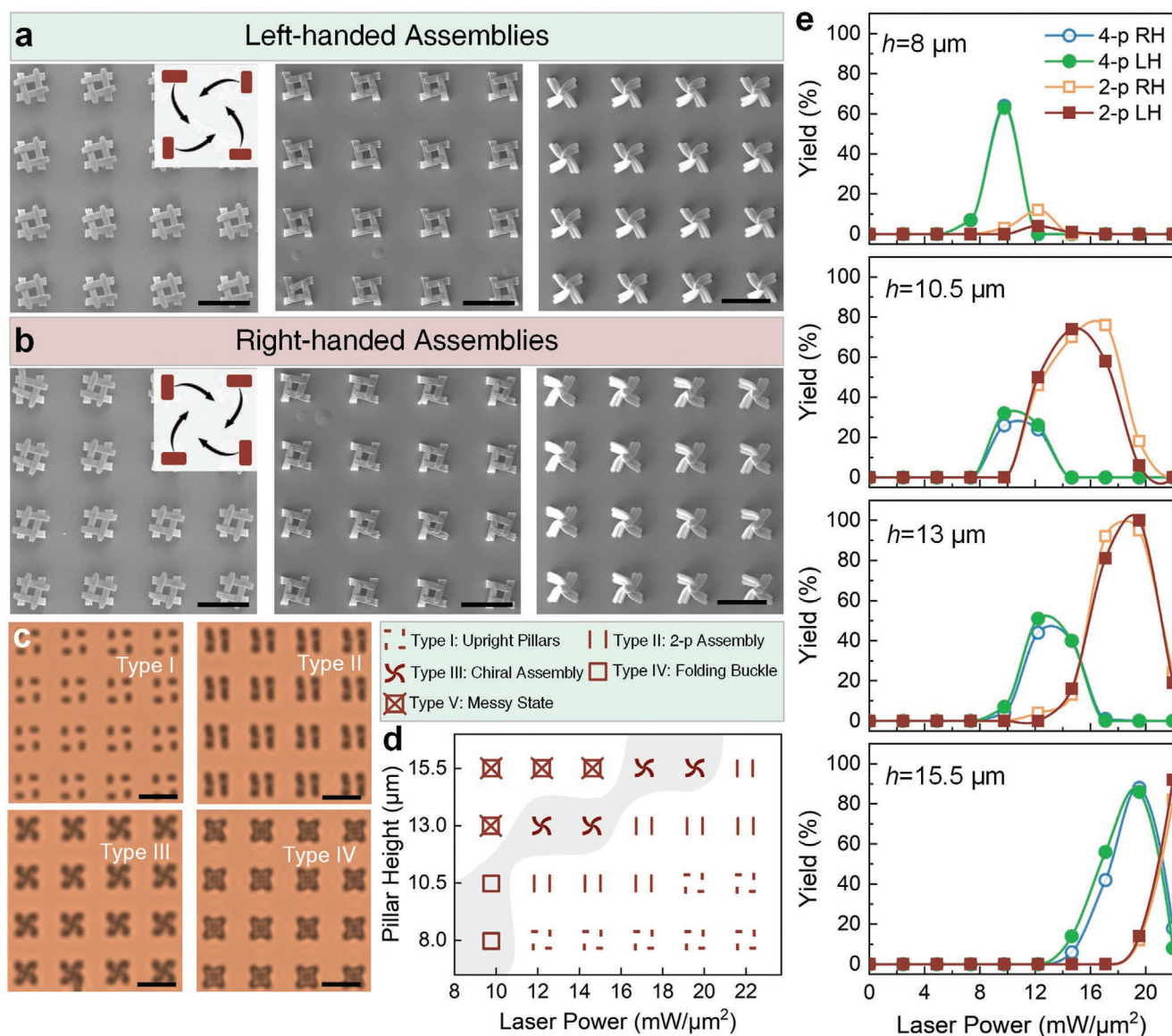
Figure 2. Varieties of assembling modes with changeable micropillar parameters: a) left-handed and b) right-handed chiral assemblies constructed with four-pillar unit cells. The pillar height in the folding buckle assemblies are 10.5 μm (left column) and 8.5 μm (middle column), respectively. The pillar height of the pinwheel-like chiral assembly is 15.5 μm (right column). Note that here two or three discrete micropillars are fabricated close to each other to obtain the anisotropic cross-section. The length–width ratio of the cross-section is 2:0.7 (major axis: 2 μm; minor axis: 0.7 μm). c) Different modes of the assemblies with varying pillar height and laser power. Scale bars: 10 μm. d) Phase diagram summarizing the modes of assemblies with different pillar height and laser power. The shaded region indicates the appropriate parameters sets for four-pillar chiral assembly formation. e) Quantitative relationship between yield ratio and laser power with different pillar heights.

are transition zones between neighboring regimes because there is a possibility that two or more assembling modes coexist within the micropillars array with the same preparation parameters.

Therefore, a series of quantitative studies are performed to characterize the yield ratio of chiral assemblies (including Type II, Type III, and Type IV), as shown in Figure 2e. In order to perform the statistical analysis on the yield ratio, 7 × 7 unit cell array of each mode is fabricated and analyzed. When the height of micropillars is 8 μm, the chiral assemblies are formed only with the low laser power (9.76 mW μm^{-2}) and the assembly type appears to be the highly ordered interlocking folding

buckles as illustrated in the middle column of Figure 2a,b. When the height of micropillars increases to 10.5 μm and the laser power remains the same at 9.76 mW μm^{-2}, the #-shaped folding buckles can be formed as shown in the left column of Figure 2a,b. With the pillar height of 10.5 μm, when the laser power increases, the stiffness of the micropillars increases accordingly, leading to the assembly modes of two-pillar chiral assembly (Type II) under the laser power from 12.2 to 17.08 mW μm^{-2}. When the pillar height is further increased to 13 μm, four-pillar pinwheel assemblies (Type III) appear when laser power ranges from 9.76 to 14.64 mW μm^{-2} and two-pillar assembly mode (Type II) predominates when the laser power is

ADVANCED
SCIENCE NEWS
www.advancedsciencenews.com

ADVANCED
MATERIALS
www.advmat.de

higher than 14.64 mW µm^{-2}. As expected, all the printed micropillars collapse when the height is increased to 15.5 µm under relatively low laser power (<14.64 mW µm^{-2}). The structural strength of the micropillars is enhanced with high laser power, therefore chiral assemblies (Type III) are formed with laser power ranging from 14.64 to 19.52 mW µm^{-2} (corresponding to the right column of Figure 2a,b). When the laser power is 21.96 mW µm^{-2}, two-pillar assemblies (Type II) are generated. The yield of the assemblies with different modes can be well explicated by the competition between meniscus-induced capillary force and elastic standing force. In brief, the chiral assemblies can be formed only with specific parameters due to the proper force coupling.

Based on the design concept of regulating the micropillar geometries and spatial topologies, diverse chiral assemblies with unprecedented complexity and hierarchical features can be created at will. Due to the excellent flexibility of femtosecond laser printing, the number of micropillars, the cross-section, and the spatial arrangements can be readily controlled. The SEM images of diverse assemblies of 6- and 12-pillar cells with different designs are shown in **Figure 3**. Figure 3a shows the chiral microstructures with six anisotropic petals in each basic unit cell (here each rectangular pillar is constructed from discrete micropillars with circular cross-section, the schematic diagram is shown in Figure S4, Supporting Information). A similar chiral assembly can be also created by anisotropic micropillars with smooth rectangular cross-section under the capillary force, as shown in Figure 3b. By changing the spatial arrangement, the six-pillar cell can be assembled into vastly different forms as shown in Figure 3c. The cooperative control over micropillar cross-section and spatial arrangement can directly influence the resultant assembly.

Furthermore, the length–width ratio (LWR) of the micropillar and the laser power for printing can also play important roles in determining the morphology of the eventual assemblies. As shown in Figure 3d–f, and Figure S5 and Video S1 (Supporting Information), the spatial arrangement of the 12 pillars is the same, the height of the micropillars is fixed to be 18 µm, and the length of the minor axis is 700 nm. Figure 3d,e shows the chiral assemblies constructed by the micropillars with the major axis of 3.5 and 4.75 µm, respectively. Because the height of the micropillars and the diameter of the unit cell are larger than the four-pillar design in Figure 2, the laser power is set to be a little higher (30 mW µm^{-2}) for these micropillars in Figure 3 in order to obtain the uniform assemblies. When the laser power is increased to 35 mW µm^{-2} (major axis of 4.75 µm), the morphology of assemblies can be also impacted as shown in Figure 3f. It is of special interest that when the laser power is further increased (40 mW µm^{-2}), a central opening can be formed due to the incomplete assembly caused by the high pillar stiffness (Figure 3g and Figure S6, Supporting Information). Moreover, the opening size of the central hole can be tuned by varying the laser power or the pillar height gradually, as shown in Figure 3h. The reversible cage-like microassembly with tunable opening provides a possible tool in future for capturing microorganism or single cell and culturing.

When the laser power is lowered below 30 mW µm^{-2}, the spiral top of the structure become more evident as shown in Figure 3i–k. Here the geometry and spatial arrangement of the

twelve micropillars are the same as that in Figure 3d, whereas the laser power is 25 mW µm^{-2}. In contrast, the chirality became weak when the laser power is increased to 35 mW µm^{-2} and the geometry remains the same (Figure 3l–n and Figure S7, Supporting Information). The twisting direction of the multipillar chiral assemblies can be well controlled. It can be seen that all the assemblies are highly ordered and rotationally symmetric, indicating that the micropillars in a unit cell are sequentially buckled to form an interlocking architecture. The various configurations of the assemblies demonstrate the ability of the LPCS strategy to prepare hierarchical chiral microstructures by exploring capillary force as the controllable driving force. Direct laser writing (DLW) has been greatly developed for high-quality chiral structures formation and dynamic 4D printing.[18] The capillarity-assisted method is anticipated to further broaden the applicability of DLW technique. The manner of building chiral microstructures using individual filaments eliminates the negative influence of voxel superposition and self-smoothing effect,[19] resulting in high-quality and reliable microassemblies. Moreover, it is noteworthy that the LPCS has the advantage of good scalability because the capillary force exists in various dimensions and the accessible chiral structures are purely determined by the pillar unit blocks. In addition, an alternative LPCS strategy is discussed in Figures S8 and S9 and Video S2 (Supporting Information) to prepare chiral assemblies using laser printing slanted micropillars with symmetric round cross-section and subsequent assembling them by capillary force.

It has been well known that the spin angular momentum (SAM, related to the circular polarization of light) of photons is widely used to probe nanoscale enantiomer's handedness characterized by circular dichroism (CD), which is a chiral-optical phenomenon arising from the strong interaction between the circularly polarized wave and the chiral molecules.[20] However, the dimension of the chiral molecules has to be around the wavelength scale for CD measurement, greatly hindering its applications in discriminating chiral structures at the microscale or mesoscale due to the size mismatching. Light carrying the orbital angular momentum (OAM) has been intensively used in the field of optical manipulation,[21] communication,[22] quantum entanglement[23] and nanofabrication.[7] In analogous to the CD measurement, the vortical dichroism (VD) is observed which originates from the difference in reflectance of incident beam with opposite OAMs on spiral microstructures. Inversely, the chiral microstructures are capable of probing the conserved optical OAMs due to the distinguishable responses. Here we show that the assembled chiral microstructures possess giant VD similar to the standard spiral surfaces. In analogous to the CD definition, the VD is given by

$$VD = 2 \times \frac{I_R - I_L}{I_R + I_L} \times 100\% \tag{4}$$

where I_R and I_L are the reflection intensities of helical microstructures under right-handed wave front (RHW) and left-handed wave front (LHW) illumination, respectively. The VD is measured by illuminating monochromatic optical vortices upright onto the chiral microassemblies, as schematically shown in **Figure 4**a. In the experimental setup, a spatial light

**ADVANCED
SCIENCE NEWS**

www.advancedsciencenews.com

**ADVANCED
MATERIALS**

www.advmat.de
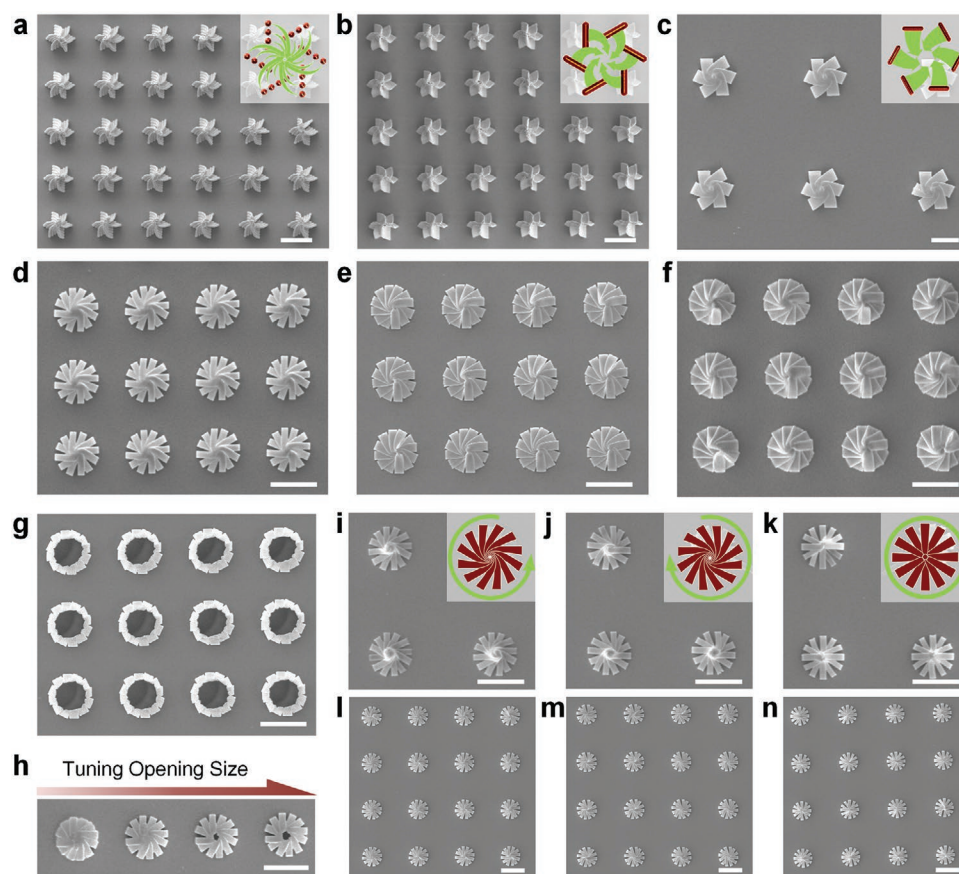
Figure 3. Collection of diverse chiral assemblies prepared by LPCS strategy. a,b) Right-handed pinwheel-like microstructures with six branches. Each branch is constructed with discrete micropillars (a) and a continuous smooth anisotropic microplate (b). c) The morphology of chiral assembly changes when changing the spatial arrangement of the six petals. Scale bars: 10 µm. d–f) 12-Pillar chiral assemblies with varying cross-section and laser power. The length–width ratios (LWRs) of the pillars are: d) 5:1 and e) 6.8:1, respectively. The laser power is 30 mW µm^{-2}. f) The pillar geometry and spatial localization is the same as that in (e) whereas the laser power is increased to 35 mW µm^{-2}. g) Assemblies with opening on the top are obtained by increasing the laser power to 40 mW µm^{-2}. The height of all the pillars in (d)–(g) is 18 µm. The opening size on the top can be tuned as shown in (h). i–k) 12-Pillar assemblies with different handedness prepared with low laser power (25 mW µm^{-2}): i) left-handed, j) right-handed, and k) achiral assemblies. l–n) Highly ordered 12-pillar assemblies with different handedness prepared with relatively high laser power (35 mW µm^{-2}): l) left-handed, m) right-handed, and n) achiral assemblies. Scale bars: 20 µm.

modulator (SLM) is utilized to modulate the incident light to carry different OAMs. Programmable computer generated holograms (CGHs) with azimuthal phase distributions are encoded on the SLM to generate optical vortices with varying topological charges l. It is worth mentioned that superposition of a blazed grating is performed onto the CGHs to readily separate the undesired zero-order beams from the optical vortices. The measured optical VD versus topological charge $|l|$ of several pairs of typical microassemblies (6-pillar, 8-pillar and 12-pillar assemblies) with opposite handedness is shown in Figure 4b–d. It is evident that the VD spectra of these chiral microstructures with opposite handedness are generally mirror-symmetric with respect to the zero line, implying good reliability of LPCS chiral microstructures with opposite handedness. It can be seen that the VD peaks occur at the same topological charge of 12 with different assemblies. The VD magnitudes can reach around ≈50% with the eight-pillar assemblies, attributing to the strong coupling between the helical wave front and slanted profile of chiral assemblies. Two peaks can be observed with the 12-pillar

assemblies, which is caused by the relatively large diameters of the unit cell and consequent extension of the interacting area between optical vortices and microstructures. The deterministic VD response makes the chiral assemblies as effective probes for differentiating the sign and topological charges of monochromatic light OAMs.

This work presents two crucial novelties from the point of view of science and applications. The first is the inventive design to harness the capillary force at the microscale for assembly of chiral microstructures. The second is that the mechanism study of chirality formation and systematical investigation on the influence parameters, which provides theoretical guidance and processing optimization for realizing highly ordered chiral microstructures.

In summary, capillarity-induced chiral self-assemblies are generated through synergistic control of the micropillars geometry and spatial topology by taking advantage of the flexibility of femtosecond laser printing. Mesoscale hierarchical assemblies constructed with building blocks of 4-, 6-, 12-pillars are
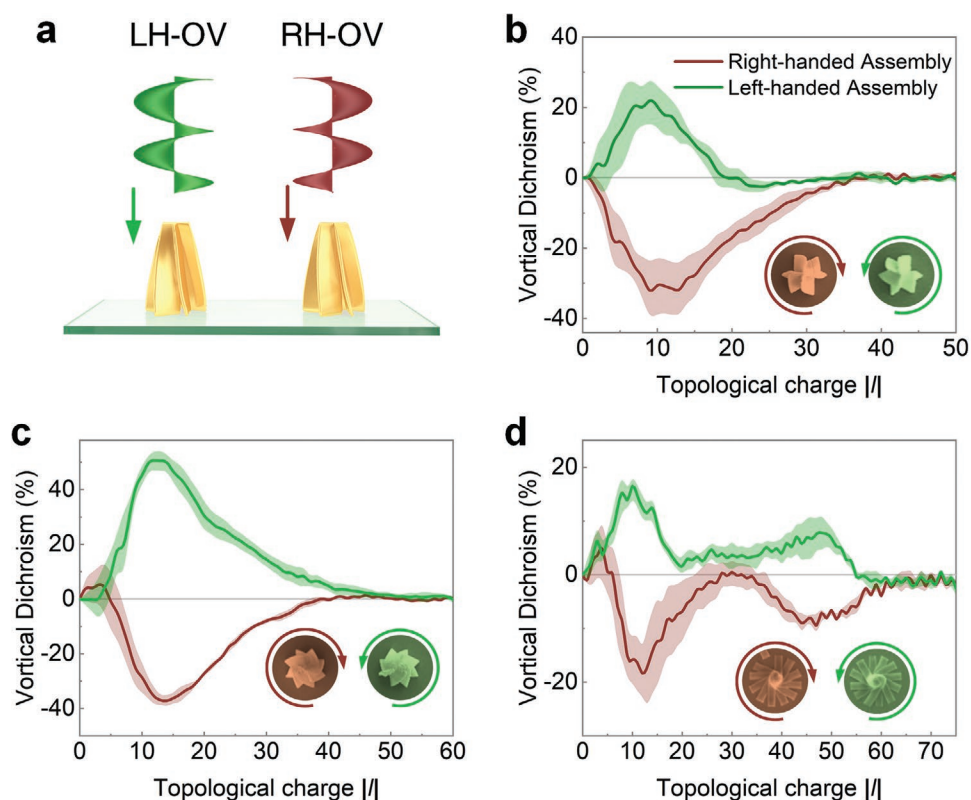
Figure 4. Vortical dichroism measurements of the chiral assemblies with opposite handedness. a) Schematic sketch of the OAM beams irradiating upright onto the chiral assembly. b–d) Measured optical vortical dichroism versus topological charge |l| of different assembled enantiomers: b) six-pillar chiral assemblies; c) eight-pillar chiral assemblies, and d) 12-pillar chiral assemblies.

obtained with predesigned handedness. High complexity and regularity of the resultant assemblies verifies that the LPCS strategy holds the great promise for fabricating ordered chiral architectures over a large range. The interfacial dynamics of the chiral assembly formation is presented for tuning the assembling modes during the liquid evaporation process by purposely changing the pillar height, cross-section, laser power and spatial topology. As a proof-of-concept demonstration, the vortical dichroism associating with the incident lights carrying opposite OAMs is exploited, unfolding new possibilities for probing the latent chiral characteristics of light including topological charges and handedness.

Experimental Section

Laser Printing System: A mode-locked Ti:sapphire ultrafast oscillator (Chameleon Vision-S, Coherent) was used as the laser source. The central wavelength of the laser was 800 nm, with a pulse duration of 75 fs and a repletion rate of 80 MHz. An oil-immersed objective lens (60×, NA = 1.35, Olympus) and a general objective lens (50 ×, NA = 0.8, Olympus) were used to focus the laser beam for flexibly regulating the polymerization degree of photoresist. The sample was immobilized on a 3D nanotranslation stage (E545, Physik Instrumente) with nanoresolution and 200 µm × 200 µm × 200 µm traveling range to precisely determine the locations of the microstructures. The exposure time of each point was controlled by an optical beam shutter (SH05, Thorlabs).

Material: A commercially available zirconium–silicon hybrid sol–gel material was used for photopolymerization (SZ2080, IESL-FORTH,

Greece). The principal characteristic of this material compared to other photoresists was the negligible shrinkage during structuring. More information about it could be seen elsewhere.[24] Before fabrication, the photoresist was placed on a hot plate at 100 °C for 45 min to remove the solvent.

Capillary Force Induced Self-Assembly: After polymerization by femtosecond laser, the sample was soaked in 1-propanol for 30 min to wash away the unprocessed material. After extraction from 1-propanol, the sample was placed in air at the ambient temperature. The micropillar array was assembled into a variety of complex 3D microarchitectures induced by capillary force generated by evaporation of the liquid remaining between neighboring pillars.

Measurement of Vortical Dichroism: The optical vortices were generated by a spatial light modulator (SLM, Pluto NIR-II, Holoeye Photonics). This liquid-crystal SLM working on a reflective mode featured 1920 × 1080 resolution, 8 µm pixel pitch, on which programmable computer-generated-holograms (CGHs) with 256 gray levels could be encoded. In order to separate the unwanted zero-order beams from the optical vortices, superposition of a blazed grating is performed. The monochromic light source was the same as that in fabrication system with a wavelength of 800 nm, except that the power was greatly attenuated to avoid any influence to the microstructure. After aligning the center of optical vortex to the chiral microstructure, the reflected intensity profiles were captured by a CCD camera (WV-BP334, Panasonic). The optical vortices with laser power of 0.5 mW was used for characterization.

Characterization of Samples: The SEM images were taken using a secondary-electron scanning electron microscope (EVO18, ZEISS) with an accelerating voltage of 5.0, 10.0, or 20.0 keV after depositing ≈10 nm of gold. The optical images were taken using an inverted microscope (DMI 3000B, Leica).

Supporting Information

Supporting Information is available from the Wiley Online Library or from the author.

Acknowledgements

Conflict of Interest

The authors declare no conflict of interest.

Keywords

[1] E. A. Valentijn, *Nature* **1990**, *346*, 153.

[2] S. J. Gerbode, J. R. Puzey, A. G. McCormick, L. Mahadevan, *Science* **2012**, *337*, 1087.

[3] S. Englander, N. Kallenbach, A. Heeger, J. Krumhansl, S. Litwin, *Proc. Natl. Acad. Sci. USA* **1980**, *77*, 7222.

[4] a) Y. Cui, L. Kang, S. Lan, S. Rodrigues, W. Cai, *Nano Lett.* **2014**, *14*, 1021; b) S. P. Rodrigues, S. Lan, L. Kang, Y. Cui, P. W. Panuski, S. Wang, A. M. Urbas, W. Cai, *Nat. Commun.* **2017**, *8*, 14602; c) Y. Chen, X. Yang, J. Gao, *Light: Sci. Appl.* **2018**, *7*, 84.

[5] a) T. Frenzel, M. Kadic, M. Wegener, *Science* **2017**, *358*, 1072; b) I. Fernandez-Corbaton, C. Rockstuhl, P. Ziemke, P. Gumbsch, A. Albiez, R. Schwaiger, T. Frenzel, M. Kadic, M. Wegener, *Adv. Mater.* **2019**, *31*, 1807742.

[6] a) Z. Wang, Y. Wang, G. Adamo, B. H. Teh, Q. Y. S. Wu, J. Teng, H. Sun, *Adv. Opt. Mater.* **2016**, *4*, 883; b) C. Wu, N. Arju, G. Kelp, J. A. Fan, J. Dominguez, E. Gonzales, E. Tutuc, I. Brener, G. Shvets, *Nat. Commun.* **2014**, *5*, 3892.

[7] J. Ni, C. Wang, C. Zhang, Y. Hu, L. Yang, Z. Lao, B. Xu, J. Li, D. Wu, J. Chu, *Light: Sci. Appl.* **2017**, *6*, e17011.

[8] L. R. MacGillivray, J. L. Atwood, *Nature* **1997**, *389*, 469.

[9] H. V. Zhang, F. Polzer, M. J. Haider, Y. Tian, J. A. Villegas, K. L. Kiick, D. J. Pochan, J. G. Saven, *Sci. Adv.* **2016**, *2*, e1600307.

[10] M. Bagiński, M. Tupikowska, G. González-Rubio, M. Wójcik, W. Lewandowski, *Adv. Mater.* **2020**, *32*, 1904581.

[11] R. P. Goodman, I. A. Schaap, C. F. Tardin, C. M. Erben, R. M. Berry, C. F. Schmidt, A. J. Turberfield, *Science* **2005**, *310*, 1661.

[12] a) J. Y. Cheng, C. A. Ross, H. I. Smith, E. L. Thomas, *Adv. Mater.* **2006**, *18*, 2505; b) J. Aizenberg, A. J. Black, G. M. Whitesides, *Nature* **1998**, *394*, 868; c) K. J. Stebe, E. Lewandowski, M. Ghosh, *Science* **2009**, *325*, 159; d) V. Flauraud, M. Mastrangeli, G. D. Bernasconi, J. Butet, D. T. Alexander, E. Shahrabi, O. J. Martin, J. Brugger, *Nat. Nanotechnol.* **2017**, *12*, 73.

[13] a) M. De Volder, S. H. Tawfick, S. J. Park, D. Copic, Z. Zhao, W. Lu, A. J. Hart, *Adv. Mater.* **2010**, *22*, 4384; b) B. Hatton, L. Mishchenko, S. Davis, K. H. Sandhage, J. Aizenberg, *Proc. Natl. Acad. Sci. USA* **2010**, *107*, 10354.

[14] B. Pokroy, S. H. Kang, L. Mahadevan, J. Aizenberg, *Science* **2009**, *323*, 237.

[15] a) H. Duan, K. K. Berggren, *Nano Lett.* **2010**, *10*, 3710; b) H. Duan, J. K. Yang, K. K. Berggren, *Small* **2011**, *7*, 2661.

[16] D. Wu, S. Z. Wu, S. Zhao, J. Yao, J. N. Wang, Q. D. Chen, H. B. Sun, *Small* **2013**, *9*, 760.

[17] Y. Hu, Z. Lao, B. P. Cumming, D. Wu, J. Li, H. Liang, J. Chu, W. Huang, M. Gu, *Proc. Natl. Acad. Sci. USA* **2015**, *112*, 6876.

[18] a) C. A. Spiegel, M. Hippler, A. Münchinger, M. Bastmeyer, C. Barner-Kowollik, M. Wegener, E. Blasco, *Adv. Funct. Mater.* **2019**, 1907615; b) Y. Hu, Z. Wang, D. Jin, C. Zhang, R. Sun, Z. Li, K. Hu, J. Ni, Z. Cai, D. Pan, X. Wang, W. Zhu, J. Li, D. Wu, L. Zhang, J. Chu, *Adv. Funct. Mater.* **2020**, *30*, 1907377; c) M. Hippler, E. Blasco, J. Qu, M. Tanaka, C. Barner-Kowollik, M. Wegener, M. Bastmeyer, *Nat. Commun.* **2019**, *10*, 232.

[19] S. C. Ligon, R. Liska, J. Stampfl, M. Gurr, R. Mülhaupt, *Chem. Rev.* **2017**, *117*, 10212.

[20] a) R. L. Dubs, S. Dixit, V. McKoy, *Phys. Rev. Lett.* **1985**, *54*, 1249; b) J. K. Gansel, M. Thiel, M. S. Rill, M. Decker, K. Bade, V. Saile, G. von Freymann, S. Linden, M. Wegener, *Science* **2009**, *325*, 1513; c) A. Kuzyk, R. Schreiber, Z. Fan, G. Pardatscher, E.-M. Roller, A. Högele, F. C. Simmel, A. O. Govorov, T. Liedl, *Nature* **2012**, *483*, 311; d) A. G. Mark, J. G. Gibbs, T.-C. Lee, P. Fischer, *Nat. Mater.* **2013**, *12*, 802; e) M. Decker, M. W. Klein, M. Wegener, S. Linden, *Opt. Lett.* **2007**, *32*, 856.

[21] D. G. Grier, *Nature* **2003**, *424*, 810.

[22] J. Wang, J.-Y. Yang, I. M. Fazal, N. Ahmed, Y. Yan, H. Huang, Y. Ren, Y. Yue, S. Dolinar, M. Tur, *Nat. Photonics* **2012**, *6*, 488.

[23] A. Mair, A. Vaziri, G. Weihs, A. Zeilinger, *Nature* **2001**, *412*, 313.

[24] A. Ovsianikov, J. Viertl, B. Chichkov, M. Oubaha, B. MacCraith, I. Sakellari, A. Giakoumaki, D. Gray, M. Vamvakaki, M. Farsari, *ACS Nano* **2008**, *2*, 2257.